Journal of
Materials Chemistry A

Materials for energy and sustainability

Accepted Manuscript

This article can be cited before page numbers have been issued, to do this please use: X. He, K. Ogata, T. Terumasa, H. Hiramatsu, T. Kamiya and T. Katase, *J. Mater. Chem. A*, 2026, DOI: 10.1039/D6TA02075E.

This is an Accepted Manuscript, which has been through the Royal Society of Chemistry peer review process and has been accepted for publication.

Accepted Manuscripts are published online shortly after acceptance, before technical editing, formatting and proof reading. Using this free service, authors can make their results available to the community, in citable form, before we publish the edited article. We will replace this Accepted Manuscript with the edited and formatted Advance Article as soon as it is available.

You can find more information about Accepted Manuscripts in the Information for Authors.

Please note that technical editing may introduce minor changes to the text and/or graphics, which may alter content. The journal's standard Terms & Conditions and the Ethical guidelines still apply. In no event shall the Royal Society of Chemistry be held responsible for any errors or omissions in this Accepted Manuscript or any consequences arising from the use of any information it contains.

ROYAL SOCIETY OF CHEMISTRY

rsc.li/materials-a

View Article Online
DOI: 10.1039/D6TA02075E

Simultaneous enhancement of power factor and suppression of thermal conductivity in bulk $TlFe_{1.6}Se_2$ via embedded atomically thin FeSe layers

Xinyi He[1,2,§], *Katsuma Ogata*[1,§], *Terumasa Tadano*[3], *Hidenori Hiramatsu*[1,4], *Toshio Kamiya*[1,4], *and Takayoshi Katase*[1,*]

[1] Materials and Structures Laboratory, Institute of Integrated Research, Institute of Science Tokyo, 4259 Nagatsuta, Midori, Yokohama 226-8501, Japan

[2] Kanagawa Institute of Industrial Science and Technology, 705-1 Shimoimaizumi, Ebina, Kanagawa 243-0435, Japan

[3] Research Center for Magnetic and Spintronic Materials, National Institute for Materials Science, 1-2-1 Sengen, Tsukuba, Ibaraki 305-0047, Japan

[4] MDX Research Center for Element Strategy, Institute of Integrated Research, Institute of Science Tokyo, 4259 Nagatsuta, Midori, Yokohama 226-8501, Japan

* Correspondence to: katase.t.aa@m.titech.ac.jp

[§]X.H. and K.O. contributed equally to this work.

Keywords: Thermoelectric material; Phonon scattering, Carrier transport; Defect

View Article Online
DOI: 10.1039/D5TA02075E

ABSTRACT: FeSe in the monolayer limit exhibits extremely large thermoelectric power factors (PF). Extending the high-PF concept from two-dimensional FeSe to bulk materials, together with lattice thermal conductivity suppression, enables higher-performance thermoelectrics. Here, layered $TlFe_{1.6}Se_2$ is identified as a model system consisting of atomically thin two-dimensional FeSe layers separated by Tl atoms; i.e., FeSe monolayers are naturally confined within a bulk crystal. This compound uniquely exhibits a transition from Fe-vacancy (V_{Fe})-ordered to -disordered states around 200 °C. Although V_{Fe}-disordered phase exhibits high electrical conductivity, carrier compensation suppresses Seebeck coefficient and limits PF. In contrast, V_{Fe}-ordered phase shows an enhanced Seebeck coefficient associated with Mott gap formation, resulting in improved PF much higher than that of bulk FeSe. The lattice thermal conductivity of V_{Fe}-ordered phase is lower than those of representative thermoelectric chalcogenides, and that of V_{Fe}-disordered phase further decreases to ~0.2 W/(m·K) at 500 °C due to V_{Fe}-induced bond heterogeneity. Consequently, the dimensionless figure of merit (ZT) of $TlFe_{1.6}Se_2$ reaches ~0.2 at 50 °C in V_{Fe}-ordered phase, which is two orders of magnitude higher than bulk FeSe. These results demonstrate that confining FeSe monolayers within a bulk crystal, alongside vacancy order–disorder control, is an effective design strategy for next-generation thermoelectrics.

View Article Online
DOI: 10.1039/D6TA02075E

1 Introduction

Thermoelectric energy conversion has been expected as a promising renewable technology for converting waste heat into electricity via the Seebeck effect.[1-3] The energy-conversion efficiency of thermoelectric materials is governed by the dimensionless figure of merit (ZT), defined as $ZT = S^2\sigma T/\kappa$, where S is the Seebeck coefficient, σ is the electrical conductivity, T is the absolute temperature, and κ is the thermal conductivity. The electrical output power is given by $S^2\sigma$, known as the power factor (PF), and the κ consists of the electronic thermal conductivity (κ_{ele}) and the lattice thermal conductivity (κ_{lat}). Achieving a high ZT requires simultaneously attaining a large S and high σ while minimizing κ. However, this requirement is fundamentally constrained by well-known trade-offs among these parameters. For example, σ and S exhibit an inverse dependence on the carrier concentration (n): increasing n enhances σ but reduces S, resulting in a maximum PF at an optimal n. Moreover, increasing σ typically raises κ_{ele} according to the Wiedemann-Franz law ($\kappa_{ele} = L\sigma T$, where L is the Lorenz number). Owing to this intricate interdependence of transport properties, realizing thermoelectric materials with high ZT remains a major challenge.[4] In contrast, κ_{lat} is largely independent of these electronic transport parameters, and materials with intrinsically low κ_{lat} are therefore well suited for achieving high ZT.

Recently, a giant PF has been reported in ultra-thin films of layered FeSe,[5] one of the high-critical-temperature (T_c) Fe-based superconductors.[6] Ultra-thin FeSe film grown on $SrTiO_3$ substrate has attracted considerable attention because it exhibits superconductivity with T_c up to 100 K,[7] dramatically higher than bulk T_c of ~9 K. When the film thickness is reduced to ~1 nm, σ increases due to interface-induced carrier doping from the $SrTiO_3$ substrate, while S also increases due to enhanced two-dimensionality and electron correlation effects. As a result, the PF reaches 260 μW/(cmK^2), a value much higher than that of practical Bi_2Te_3 at room temperature (RT).[5] Furthermore, the PF of ultra-thin FeSe increases to 13,000 μW/(cmK^2) at

View Article Online
DOI: 10.1039/D6TA02075E

a reduced temperature of 50 K. Assuming κ~5 W/(mK), similar to bulk Fe-based superconductors,[8,9] the *ZT* of the ultra-thin FeSe is estimated to be ~1.5 at 280 K. However, the excellent PF and *ZT* values appears only in the ultra-thin limit, which makes these films unsuitable for thermoelectric power generation. It would therefore be more interesting if such high PF could be achieved throughout the bulk phase of FeSe. In addition, FeSe has been reported to exhibit a relatively high κ_{lat} ~4.5 W/(mK) at RT in polycrystalline samples,[10] which is nearly three times higher than that of Bi_2Te_3.[11] Therefore, reducing the κ_{lat} in FeSe is also crucial for realizing its potential as a high-performance thermoelectric material.

To overcome the limitations of ultra-thin FeSe, we herein focus on a layered $A_{1-x}Fe_{2-y}Se_2$ (*A* = alkali metals and Tl), which can be regarded as a natural bulk analogue of FeSe monolayers. This compound crystallizes in a tetragonal $ThCr_2Si_2$-type structure composed of alternately stacked FeSe layers and *A*-ion layers along the *c*-axis (**Figure 1a**).[12] This crystal structure intrinsically contains atomically thin FeSe monolayers within a bulk crystal. The FeSe layers in $A_{1-x}Fe_{2-y}Se_2$ possess an identical crystal lattice to that of FeSe, in which Fe atoms form a square lattice and Se atoms occupy apical positions of edge-shared $FeSe_4$ tetrahedra. The thickness of the FeSe layer in $TlFe_{1.6}Se_2$ is ~3.0 Å, corresponding to a single FeSe slab, which is significantly thinner than the ~1 nm minimum thickness reported for ultrathin FeSe films.[5] Notably, Fe sites intrinsically contain vacancies (V_{Fe}), forming a $\sqrt{5} \times \sqrt{5} \times 1$ supercell of the $ThCr_2Si_2$-type structure (**Figure 1b**). Upon heating, the arrangement of V_{Fe} undergoes a transition between ordered and disordered states at ~500 K. Theoretical calculations have suggested that the V_{Fe}-ordered $A_{1-x}Fe_{2-y}Se_2$ is a Mott insulator with a Mott gap of ~100 meV,[13,14] and the gap has been experimentally confirmed to be ~430 meV.[15] The V_{Fe}-ordered Mott insulator phase also exhibits long-range antiferromagnetic (AFM) order with a Néel temperature as high as 470−560 K.[12] In contrast, by tuning the deficiencies at *A* site and Fe site, the $A_{1-x}Fe_{2-y}Se_2$ can exhibit superconductivity with T_c = 30 K.[16,17] Note that the electronic transport in $A_{1-x}Fe_{2-y}Se_2$ is mainly governed by the FeSe layers, where the

View Article Online
DOI: 10.1039/D5TA02075E

electronic states near the Fermi level are dominated by Fe 3d orbitals.[14] As a result, the contribution of *A*-site ions to the electron transport is relatively limited. Based on these characteristics, $A_{1-x}Fe_{2-y}Se_2$ is expected to exhibit a high PF owing to its two-dimensional FeSe layers naturally embedded within the bulk crystal. In particular, strong electron correlation may lead to an enhanced *S*, while the presence of the ordered and disordered V_{Fe} defects is expected to promote phonon scattering and thereby reduce κ_{lat}.

In this paper, we investigate the electronic and phonon transport properties of bulk polycrystalline layered $TlFe_{1.6}Se_2$ as a model system to clarify the effectiveness of embedded two-dimensional FeSe layers in enhancing thermoelectric performance. This compound is much more stable in air than other $A_{1-x}Fe_{2-y}Se_2$ phases (*A* = K, Rb, Cs),[18] and a fully V_{Fe}-ordered phase with high chemical homogeneity can be obtained due to the lower vapor pressure of Tl compared with those of alkali metals.[19] We demonstrate that the PF of $TlFe_{1.6}Se_2$ is significantly higher than bulk FeSe; furthermore, $TlFe_{1.6}Se_2$ exhibits an exceptionally low κ_{lat}, with both the electronic and phonon transport properties strongly modulated by the V_{Fe} ordering and disordering, resulting in an enhanced *ZT*.

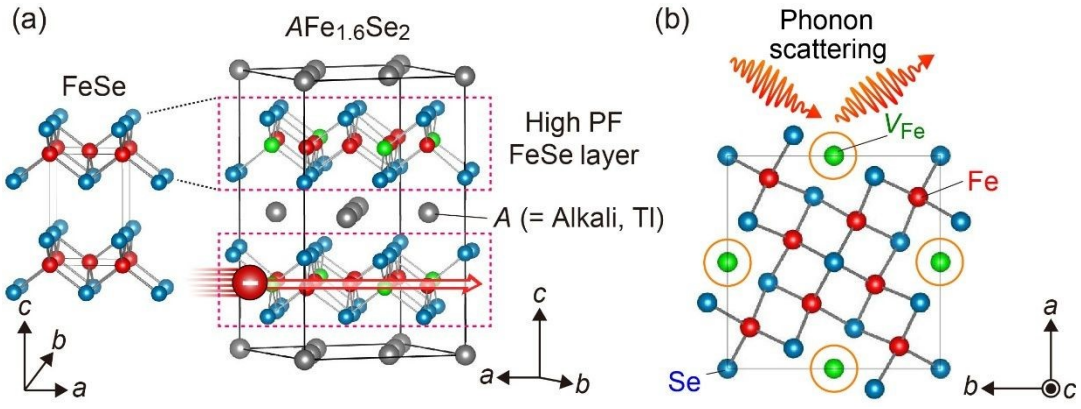

Figure 1. Crystal structure of layered $AFe_{1.6}Se_2$ (*A* = Alkali metals, Tl) with an Fe-vacancy (V_{Fe}) ordered structure, viewed along (a) [120] and (b) [001] directions. The spheres represent Tl (gray), Fe (red), Se (blue) atoms, and V_{Fe} sites (green). The structure consists of FeSe layers, crystallographically equivalent to high-power-factor (PF) FeSe monolayers, sandwiched by *A*-

View Article Online
DOI: 10.1039/D6TA02075E

ion layers. The Fe sites intrinsically host V_{Fe}, which undergo an order–disorder transition upon heating to ~500 K, which is expected to enhance phonon scattering. The coexistence of FeSe layers with intrinsic V_{Fe} defects is expected to enable a high PF together with low lattice thermal conductivity.

2 Synthesis and characterization

2.1 Synthesis

FeSe was synthesized by a solid-state reaction using Fe powder (purity: 99.999%, Kojundo Chemical Lab.) and Se powder (purity: 99.999%, Kojundo Chemical Lab.), mixed at the molar ratio of Fe : Se = 1 : 1. The mixed powders were sealed in an evacuated silica-glass ampule and annealed at 400 °C for 5 h, followed by annealing at 800 °C for 10 h. $TlFe_{1.6}Se_2$ was prepared by a solid-state reaction of fine pieces of Tl metal (purity:99.9%, Aldrich) and powders of FeSe and Se. The precursors were mixed in a stoichiometric atomic ratio of Tl : FeSe : Se = 1 : 1.6 : 0.4 and sealed in an Ar-filled stainless-steel tube. The mixture was reacted at 400 °C for 5 h and subsequently at 650 °C for 10 h.[20] The resulting FeSe and $TlFe_{1.6}Se_2$ powders were thoroughly ground and sintered into pellets by a hot-press method at 500 °C for 10 min. All reagents and products were handled in a glove box filled with dry Ar gas (dew point <−80 °C, oxygen concentration < 1 ppm).

2.2 Characterization

Crystalline phases were examined by X-ray diffraction (XRD) in the Bragg−Brentano geometry using a Cu Kα radiation source (MiniFlex600, Rigaku Co.). The lattice parameters were refined by the Pawley method using the TOPAS ver. 4.2 program (Bruker AXS GmbH). The microstructure and chemical compositions (i.e., atomic ratios of Tl, Fe, and Se) of the samples were characterized using an electron probe micro-analyzer (EPMA).

σ and S were simultaneously measured using a ZEM-3 (ULVAC-RIKO, Inc.) under a He

View Article Online
DOI: 10.1039/D5TA02075E

atmosphere. The S was obtained by giving a temperature difference (ΔT), the thermoelectromotive force (ΔV) and ΔT were measured simultaneously, and S was determined from the slope of the ΔV–ΔT plots. Pt electrodes deposited by sputtering were used to form ohmic contacts. κ was obtained from $\kappa = D \cdot C \cdot d$, where the thermal diffusivity (D) was measured in an Ar atmosphere by the laser flash method (LFA 457, NETZSCH), the specific heat capacity (C) was measured by differential scanning calorimetry (DSC), and the sample density (d) was determined from the mass and geometric dimensions of the pellets. κ_{ele} was calculated using $\kappa_{ele} = LT\sigma$. L was calculated based on a single-parabolic-band model as

$$L = \left(\frac{k_B}{e}\right)^2 \left(\frac{(r+\frac{7}{2})F_{r+5/2}(\eta)}{(r+\frac{3}{2})F_{r+\frac{1}{2}}(\eta)} - \left[\frac{(r+\frac{5}{2})F_{r+3/2}(\eta)}{(r+\frac{3}{2})F_{r+1/2}(\eta)}\right]^2 \right),$$ [21]

where k_B is Boltzmann constant. Here, the reduced Fermi energy (η) was obtained based on the free carrier model using the measured S as $S = \frac{k_B}{e}\left(\frac{(r+\frac{5}{2})F_{r+3/2}(\eta)}{(r+\frac{3}{2})F_{r+1/2}(\eta)} - \eta\right)$ with the Fermi integral defined as $F_n(\eta) = \int_0^\infty \frac{\chi^n}{1+e^{\chi-\eta}} d\chi$, where $r = -1/2$ is the scattering factor.[22] κ_{lat} was obtained by subtracting κ_{ele} from the total κ, i.e., $\kappa_{lat} = \kappa - \kappa_{ele}$. The σ and S were measured in the in-plane direction of the hot-pressed pellets, while the κ was measured along the out-of-plane direction.

2.3 Theoretical analysis

First principles calculations were conducted using the projector-augmented wave (PAW) method as implemented in the Vienna Ab initio Simulation Package (VASP).[23,24] Tl [5d6s6p], Fe [3d4s], and Se [4s4p] orbitals were treated as valence states. Variable-cell structural optimizations were performed using the Perdew–Burke–Ernzerhof functional adapted for solids (PBEsol) functional,[25] with a plane-wave cutoff energy of 550 eV, the convergence criteria of 10^{-6} eV for the energy and 0.01 eV/Å for the force, and a Γ-centered k-mesh with a k-spacing of 0.1 $Å^{-1}$. Phonon calculations were performed by using ALAMODE codes.[26,27] For FeSe, a 4 × 4 × 2 supercell containing 192 atoms was employed to compute the interatomic force

View Article Online
DOI: 10.1039/D5TA02075E

constants (IFCs). For $TlFe_{1.6}Se_2$, a 2 × 2 × 2 supercell with 368 atoms was used to obtain the harmonic IFCs, whereas a 1 × 1 × 1 unit-cell with 46 atoms was used to evaluate the anharmonic IFCs. The harmonic IFCs were fixed to the values determined by the finite-displacement approach,[28,29] and the anharmonic IFCs up to the sixth order were estimated by the compressive sensing lattice dynamics. We included all allowed interactions for the harmonic IFCs, all third-order IFCs within a 12-bohr cutoff radii, and all fourth- to sixth-order IFCs within an 8-bohr cutoff radii. Density functional theory (DFT) calculations used to obtain the energies and the forces were performed using the PBEsol functional with a plane-wave energy cutoff of 400 eV, and an energy convergence criterion of 10^{-8} eV. Finite-temperature phonon dispersions were computed by using the self-consistent phonon (SCPH) approach.[30] κ_{lat} was determined by considering the Peierls term, which was obtained by solving the Peierls–Boltzmann transport equation (PBTE) under the single-mode relaxation time approximation, and the coherent term following the unified formula.[31] Phonon-isotope scatterings were considered.[32] The convergence of κ_{lat} with respect to the q-point mesh was verified using a 7×7×7 grid for $TlFe_{1.6}Se_2$ and a 15×15×10 grid for FeSe in the PBTE calculations.

3 Results and discussion

3.1 Electrical transport properties

Crystal structures and microstructure characterizations are summarized in **Figure 2** and **Figures S1, S2** of Supporting Information. It was confirmed that $TlFe_{1.6}Se_2$ adopted V_{Fe}-ordered crystal structure with space group of $I4/m$ (**Figure 2a**) and FeSe crystallized in a PbO-type α-phase with space group of $P4/nmm$ at RT (**Figure S2**). Upon heating the $TlFe_{1.6}Se_2$ bulk sample, a transition from V_{Fe}-ordered structure to V_{Fe}-disordered structure (space group: $I4/mmm$) was observed in T range of 100–200 °C (**Figure 2b**). At higher T, the V_{Fe}-disordered phase became stable.[33] When cooled back to RT, the V_{Fe}-ordered phase reappeared, indicating

View Article Online
DOI: 10.1039/D6TA02075E

a reversible structural transition. The relative density of the sintered bulk samples was ~96%. A minor secondary phase of Fe_7Se_8 (~2.6 mol%) was detected in the FeSe sample (**Figure S2**). Although Fe_7Se_8 is a ferromagnetic metallic phase with a vacancy-ordered NiAs-type crystal structure[34] and may in principle contribute to electrical transport, its small fraction suggests that its influence on the overall transport properties is expected to be limited.

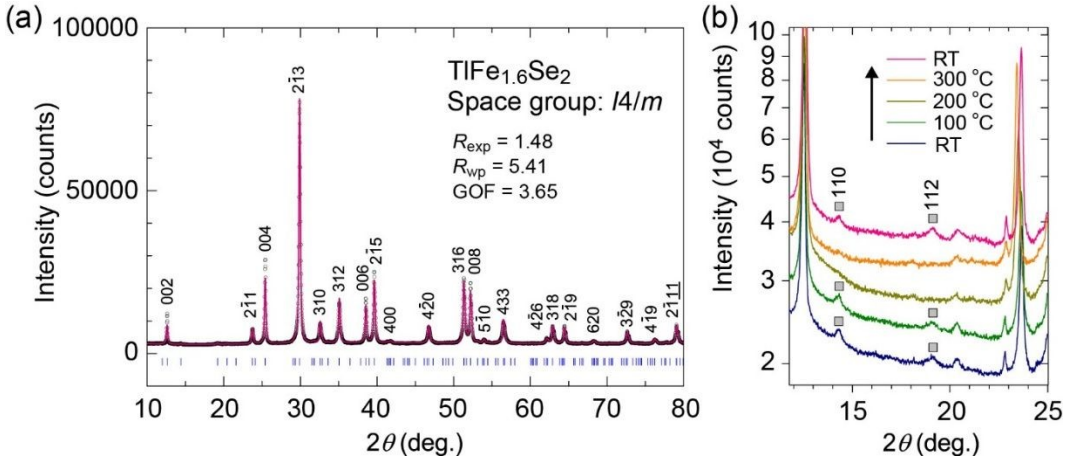

Figure 2. (a) XRD pattern of $TlFe_{1.6}Se_2$ bulk sample at RT. (b) Enlarged view of XRD patterns measured at different T. In the T range from RT to 100 °C, superlattice diffraction peaks of 110 and 112, originating from V_{Fe} ordering, were clearly observed. On the other hand, these peaks disappeared between 200 °C and 300 °C, indicating that V_{Fe} disordering occurred in the T range. Upon cooling back to RT, the superlattice reflections reappeared, demonstrating that the V_{Fe} ordered structure reversibly recovered at RT.

Figure 3 compares the T dependences of electrical transport properties of $TlFe_{1.6}Se_2$ and FeSe bulk polycrystals. FeSe tends to transform to the NiAs-type β-phase at ~300 °C,[35] and accordingly, all measurements were performed below this temperature to retain the α-phase FeSe. For FeSe, σ exhibited only a slight T dependence; it increased from 1.7×10^5 S/cm at 50 °C to 1.9×10^5 S/cm at 290 °C (upper panel of **Figure 3a**). At 50 °C, FeSe showed a small positive S of 10 μV/K (**Figure 3b**), which is consistent with the previously reported p-type

conduction inferred from Hall-effect measurements.[36] Upon heating, however, the absolute value of S ($|S|$) gradually decreased and the sign eventually became negative around 200 °C, reaching –4 μV/K at 290 °C. This sign reversal suggests that the dominant carrier type changes with T, which is reasonable given that metallic FeSe is a multiple-band system.[36] In contrast, $TlFe_{1.6}Se_2$ showed a significant increase in σ in the T range of 150–200 °C, rising from 402 S/cm in the V_{Fe}-ordered phase at 50 °C to 1064 S/cm at 595 °C upon the transition to the V_{Fe}-disordered phase (lower panel of **Figure 3a**). Upon cooling, σ reversibly returned to its original value, reflecting the reversibility of the V_{Fe} order–disorder transitions. The sign of S in $TlFe_{1.6}Se_2$ was negative over the entire T range, indicating dominant electron conduction (**Figure 3b**). In $TlFe_{1.6}Se_2$, V_{Fe} ordering induces a reconstruction of the electronic structure, associated with antiferromagnetic ordering and the opening of a band gap. The n-type behavior should not be simply attributed to Tl intercalation, because the nominal composition is charge balanced. Rather, it is more likely related to the reconstructed electronic structure associated with V_{Fe} ordering, possibly together with slight off-stoichiometry such as reduced V_{Fe} concentration or Se deficiency. At 50 °C, $TlFe_{1.6}Se_2$ exhibited a large $|S|$ value of 110 μV/K; however, once the V_{Fe} order was lost through the phase transition, $|S|$ decreased substantially around 150 °C and remained almost constant at ~34 μV/K above 200 °C. This behavior can be attributed to the collapse of the Mott gap upon V_{Fe} disordering, which leads to partial compensation between electron and hole contributions and consequently reduces the S.

As reliable Hall voltage could not be obtained by Hall effect measurements, the carrier mobility was estimated as the weighted mobility (μ_w), calculated from σ and S using

$$\mu_w = \frac{3h^3\sigma}{8\pi e(2m_e k_B T)^{3/2}}\left[\frac{\exp\left[\frac{|S|}{k_B/e}-2\right]}{1+\exp\left[-5\left(\frac{|S|}{k_B/e}-1\right)\right]}+\frac{\frac{3}{\pi^2}\frac{|S|}{k_B/e}}{1+\exp\left[5\left(\frac{|S|}{k_B/e}-1\right)\right]}\right],$$

where m_e is the free electron mass, k_B is the Boltzmann constant, h is the Planck constant, e is the elementary charge.[37] The μ_w is related to the drift mobility (μ) through $\mu_w \approx \mu\left(\frac{m^*_{DOS}}{m_e}\right)^{3/2}$,

View Article Online
DOI: 10.1039/D6TA02075E

where m^*_{DOS} is density of state effective mass. Using μ_w, the weighted carrier concentration was calculated as $n_w = \frac{\sigma}{e\mu_w}$. In the V_{Fe}-ordered phase, $TlFe_{1.6}Se_2$ exhibited a high μ_w of 60 $cm^2/(V \cdot s)$ at 50 °C, whereas the μ_w markedly decreased through the transition to the V_{Fe}-disordered phase, reaching to 8 $cm^2/(V \cdot s)$ at 595 °C. This reduction is likely associated with enhanced carrier scattering induced by the V_{Fe} disorder. The n_w in the V_{Fe}-ordered phase was ~4.3×10^{19} cm^{-3}, but it increased sharply during the phase-transition and then continued to increase gradually in the V_{Fe}-disordered phase, reaching ~8.0×10^{20} cm^{-3}. This behavior is consistent with the collapse of the Mott gap upon V_{Fe} disordering. These results suggest that both σ and S undergo pronounced changes in response to the transition between V_{Fe} ordered and disordered states, accompanied by changes in the electronic structure. **Figures 3d** summarize the T dependences of PF (= $S^2\sigma$) for $TlFe_{1.6}Se_2$ and FeSe bulk samples. Bulk FeSe exhibited a small S, resulting in low PF over the entire T range. In contrast, $TlFe_{1.6}Se_2$ showed a pronounced increase in PF in the V_{Fe}-ordered phase, reaching 5.2 μW/(cmK^2) at 50 °C, which is 30 times higher than that of bulk FeSe. Above 200 °C, where the V_{Fe}-disordered phase was stabilized, PF was reduced to ~1.0 μW/(cmK^2). These results demonstrate that $TlFe_{1.6}Se_2$, which contains FeSe monolayers embedded within the bulk crystal, can realize a substantially larger PF than bulk FeSe, with its electrical transport properties strongly modulated by the transition between V_{Fe} ordered and disordered states.

View Article Online
DOI: 10.1039/D6TA02075E

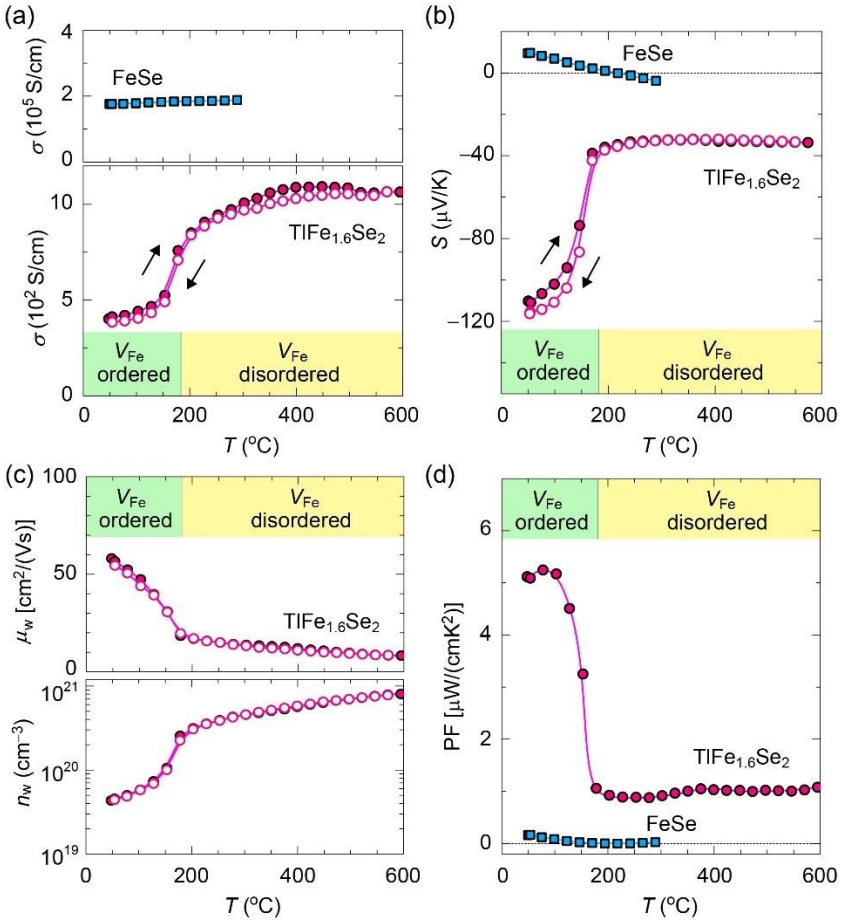

Figure 3. (a,b) T dependence of (a) electrical conductivity (σ) and (b) Seebeck coefficient (S) for FeSe and $TlFe_{1.6}Se_2$ polycrystals. (c) T dependence of weighted mobility (μ_w) and weighted carrier concentration (n_w) for $TlFe_{1.6}Se_2$ polycrystal. (d) T dependences of power factor (PF) for $TlFe_{1.6}Se_2$ and FeSe polycrystals. The green and yellow regions indicate the T ranges where the V_{Fe}-ordered phase and the V_{Fe}-disordered phase are stabilized in $TlFe_{1.6}Se_2$, respectively.

3.2 Thermal and thermoelectric properties

Next, we investigated the thermal transport properties of $TlFe_{1.6}Se_2$ and FeSe polycrystals. The T dependences of the thermal diffusivity and specific heat capacity are summarized in **Figures S3a,b** of Supporting Information. Because the specific heat capacity in $TlFe_{1.6}Se_2$ exhibited a peak near the phase-transition temperature (125–200 °C), data in this region were excluded from the analysis of κ. **Figure 4a** shows the T dependence of the total κ. FeSe

View Article Online
DOI: 10.1039/D5TA02075E

exhibited a κ value of 3.2 W/(m·K) at 50 °C, which gradually increased with increasing T and reached 4.1 W/(m·K) at 300 °C. In contrast, $TlFe_{1.6}Se_2$ showed a much lower κ of 0.8 W/(m·K) at 50 °C, remaining nearly constant up to ~125 °C. After the transition to the V_{Fe}-disordered phase, κ slightly increased to 1.0 W/(m·K) and then increased gradually, reaching 1.5 W/(m·K) at 500 °C. We next discuss thermal transport properties by separating electronic and lattice contributions. As shown in **Figure S3c** of Supporting Information, the κ_{ele} is very large in FeSe than $TlFe_{1.6}Se_2$ due to its higher σ, and therefore plays a dominant role in determining κ. **Figure 4b** compares the T dependence of the κ_{lat} (= $\kappa - \kappa_{ele}$), in comparison with the typical high-performance thermoelectric materials, including $(Bi_{0.5}Sb_{1.5})Te_3$,[38] $(Pb_{0.98}K_{0.02})(Te_{0.15}Se_{0.85})$,[39] $(Ge_{0.9}In_{0.015}Cu_{0.125})Te$,[40] Cu_2Se,[41] and SnSe[42] polycrystals. FeSe exhibited a κ_{lat} value of 1.8 W/(m·K) at 50 °C, which gradually decreased with increasing T and reached 1.4 W/(m·K) at 300 °C. In contrast, $TlFe_{1.6}Se_2$ showed an extremely low κ_{lat} of 0.7 W/(m·K) at 50 °C in the V_{Fe}-ordered phase, where κ_{lat} exhibited a weak T dependence and remained nearly constant. After the transition to the V_{Fe}-disordered phase, κ_{lat} decreased further to 0.4 W/(m·K) at 200 °C and ~0.2 W/(m·K) at 500 °C. In addition, these values are lower than those of high-performance thermoelectric materials with intrinsically low κ_{lat}, and are comparable to the lowest κ_{lat} values reported for layered SnSe polycrystals.[42] Therefore, $TlFe_{1.6}Se_2$, containing FeSe layers with V_{Fe} order–disorder structures, is demonstrated to achieve extremely low κ_{lat}.

Here, the Lorenz number (L) for κ_{ele} was estimated using a single-parabolic-band model with a scattering parameter of $r = -1/2$. Since $TlFe_{1.6}Se_2$ is a multiband Mott system with strong electron correlations, L depends on the Fermi level, effective mass and the r, which are difficult to be determined uniquely because of the complex electronic structure and the uncertainty in the dominant scattering mechanism. Then, we evaluated the L over a broad physically reasonable range of r (−1/2 to 2) and Fermi level. For the V_{Fe}-ordered phase ($n = 4.2\times10^{19}$ cm^{-3}), L varies within 1.5–2.8×10^{-8} WΩ/K^2, corresponding to an uncertainty of ±30–40%. This leads to a variation of κ_{ele} from 0.05 to 0.11 W/mK (nominal value: 0.084 W/mK), resulting in

View Article Online DOI: 10.1039/D5TA02075E

κ_{lat} ranging from 0.71 to 0.79 W/mK (nominal value: 0.74 W/mK), indicating a relatively limited uncertainty. In contrast, for the V_{Fe}-disordered phase with a higher carrier concentration ($n = 6.0 \times 10^{20}$ cm^{-3}), the L becomes much less sensitive to model parameters and converges to a narrow range of 2.4–2.5 $\times 10^{-8}$ WΩ/K^2, close to the degenerate limit. In this case, κ_{ele} is ~1.01 W/mK, with a variation of less than ±0.05 W/mK, leading to only minor alternations in κ_{lat} (~0.27 W/mK). Although the exact value of L depends on the model assumptions, the resulting uncertainty in κ_{lat} remains limited. Therefore, even when this uncertainty is taken into account, $TlFe_{1.6}Se_2$ exhibits intrinsically low κ_{lat}.

Based on the electronic and thermal transport properties discussed above, we evaluated the overall thermoelectric performance of $TlFe_{1.6}Se_2$ and FeSe (**Figure 4b**). Bulk FeSe exhibited both a small S and a high κ, resulting in low ZT over the entire T range, consistent with its metallic electronic structure. In contrast, $TlFe_{1.6}Se_2$ showed a pronounced increase of ZT in the V_{Fe}-ordered phase, reaching ~0.2 at 50 °C, which is two orders of magnitude higher than that of bulk FeSe, whereas ZT was limited to ~0.05 in the V_{Fe}-disordered phase at $T >$ 200 °C. To clarify the origin of this strong contrast in ZT between the V_{Fe}-ordered and V_{Fe}-disordered phases, the relative change in ZT across the transition was analyzed by decomposing ZT into contributions from individual transport parameters. Taking the logarithm of $ZT = S^2\sigma T/\kappa$, we obtain $\Delta\log(ZT) = \Delta\log(\sigma) + 2\Delta\log(S) + \Delta\log(T) - \Delta\log(\kappa)$, which are the approximations of relative differences, $\frac{\Delta ZT}{ZT} \sim \frac{\Delta\sigma}{\sigma} + \frac{2\Delta S}{S} + \frac{\Delta T}{T} + \frac{\Delta\kappa}{\kappa}$. Here, the contributions are evaluated using logarithmic differences, defined as $\Delta\log(X) = \log(X_{\mathrm{ordered}}) - \log(X_{\mathrm{disordered}})$, which represents the change in each parameter across the transition. **Figure 4c** summarizes the changes in each transport parameter between the V_{Fe}-ordered phase at 50 °C and the V_{Fe}-disordered phase at 400 °C. These temperatures were chosen because they lie sufficiently far from the order–disorder transition, ensuring high phase purity in the fully V_{Fe}-ordered and fully V_{Fe}-disordered states, respectively. This allows us to compare the intrinsic

View Article Online
DOI: 10.1039/D5TA02075E

transport properties of the pure phases. Positive values indicate quantities that are enhanced in the V_{Fe}-ordered phase and therefore contribute positively to the increase in *ZT*, whereas negative values indicate factors that reduce *ZT*. Although the κ_{lat} is effectively reduced in the V_{Fe}-disordered phase, the overall contribution of total κ to *ZT* is slightly negative. This is because the transition to a metallic state simultaneously leads to a substantial increase in the κ_{ele}, which compensates the benefit of the reduced κ_{lat}. In contrast, *S* exhibits the largest positive contribution, indicating that the enhancement of *ZT* in the V_{Fe}-ordered phase is predominantly driven by the large *S* associated with the opening of the Mott gap. To assess possible effects arising from the large temperature difference in the above comparison, *ZT* decomposition analysis was also performed with a closer temperature difference —125 °C for the ordered phase and 225 °C for the disordered phase (**Figure S4**). The results confirm that the overall conclusion remains unchanged; the dominant contribution to the *ZT* enhancement arises from the increase of *S*. These results demonstrate that V_{Fe} ordering in layered $TlFe_{1.6}Se_2$ enables a favorable balance between electronic and thermal transport, allowing relatively large PF and *ZT* values to be realized in bulk form.

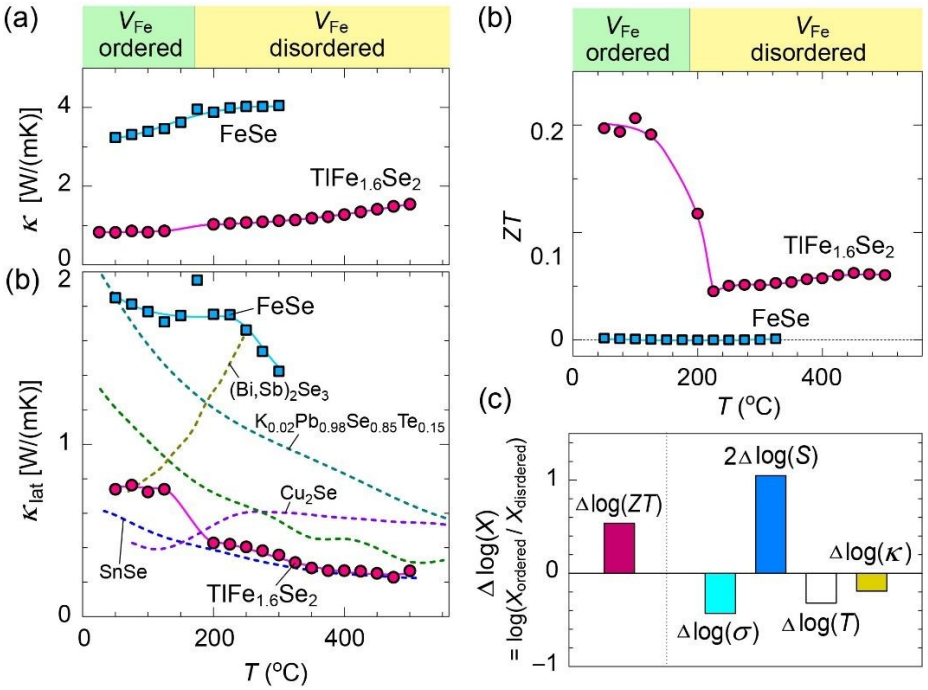

View Article Online
DOI: 10.1039/D6TA02075E

Figure 4. T dependence of (a) κ and (b) κ_{lat} for $TlFe_{1.6}Se_2$ and FeSe polycrystals. For comparison, the κ_{lat} vs. T curves of typical high-performance thermoelectric materials, including $(Bi_{0.5}Sb_{1.5})Te_3$,[38] $(Pb_{0.98}K_{0.02})(Te_{0.15}Se_{0.85})$,[39] $(Ge_{0.9}In_{0.015}Cu_{0.125})Te$,[40] Cu_2Se,[41] and SnSe[42] polycrystals, are also shown in (b). (c) T dependences of dimension-less figure of merit (ZT) for $TlFe_{1.6}Se_2$ and FeSe polycrystals. (d) Decomposition of the contributions in the ZT change across the V_{Fe} order–disorder transition, evaluated between the V_{Fe}-ordered phase at 50 °C and the V_{Fe}-disordered phase at 400 °C. Here, $\Delta\log(X) = \log(X_{ordered}/X_{disordered})$; positive (negative) values indicate parameters that enhance (reduce) ZT in the V_{Fe}-ordered phase.

To further elucidate the underlying mechanism responsible for the low κ_{lat} in $TlFe_{1.6}Se_2$, we conducted first-principles anharmonic lattice dynamics (ALD) calculations, as implemented in the ALAMODE code.[26,27] We first calculated the harmonic phonon dispersion of $TlFe_{1.6}Se_2$, shown as the dotted black lines in **Figure 5a**. Imaginary modes appear at the X and R points, indicating that the structure is dynamically unstable at $T = 0$ K within the harmonic approximation. To account for the temperature effect, SCPH calculations were performed. At $T = 300$ K, as shown by the solid blue lines in **Figure 5a**, all phonon frequencies become positive, meaning that the previously imaginary modes are stabilized after including the temperature-induced anharmonic correction. $TlFe_{1.6}Se_2$ exhibits a large number of phonon branches with strong mode entanglement (left panel of **Figure 5a**). The acoustic phonons and the low-frequency optical phonons up to ~2.5 THz exhibit relatively flat dispersions, indicating low phonon group velocities and the suppression of heat transport. The partial phonon density of states (DOSs) projected on each element for V_{Fe}-ordered $TlFe_{1.6}Se_2$ at $T = 300$ K is shown in the right panel of **Figure 5a**. The phonon DOS reveals that vibrations of the heavy Tl atoms predominantly contribute to the low-frequency phonon modes below ~2 THz. These Tl-derived optical modes exhibit extremely flat dispersions and strongly overlap with the acoustic branches, indicating highly localized vibrations associated with weak coupling between the Tl atoms and

View Article Online
DOI: 10.1039/D5TA02075E

the Fe–Se framework. In contrast, the higher-frequency phonon branches are mainly associated with vibrations of Fe and Se atoms. For comparison, the phonon dispersion and partial phonon DOS of FeSe at T = 300 K are shown in **Figure 5b**. FeSe exhibits a much simpler phonon spectrum with fewer but strongly dispersive branches (left panel of **Figure 5b**), consistent with its relatively simple crystal structure. While the phonon dispersions along the out-of-plane Γ–Z direction are relatively weak, much stronger dispersions are observed along the in-plane Γ–X and Γ–M direction, extending up to ~5 THz. The broad frequency distribution of the Fe–Se vibrational modes in the partial phonon DOSs (right panel of **Figure 5b**) reflects the strong Fe–Se bonding and is consistent with the highly dispersive phonon branches. Compared with bulk FeSe, the Fe–Se phonon branches in $TlFe_{1.6}Se_2$ exhibit reduced dispersion and stronger mode entanglement, reflecting the reduced symmetry and structural complexity of the FeSe layers caused by V_{Fe} and interlayer Tl atoms.

We subsequently calculated κ_{lat} by solving the Peierls–Boltzmann transport equation (PBTE) within the relaxation time approximation. **Figures 5c,d** present the anisotropic κ_{lat} components along the in-plane (*xx* and *yy*) and the out-of-plane (*zz*) directions for $TlFe_{1.6}Se_2$ and FeSe as a function of T, considering the contribution from the coherent term. The effect of the coherent contribution on T dependence of κ_{lat} is shown in **Figure S5** of Supporting Information. The κ_{lat} for $TlFe_{1.6}Se_2$ was calculated based on the ordered structure and is therefore shown only in the low temperatures. In layered FeSe, the pronounced structural anisotropy leads to a strong crystallographic-direction dependence of κ_{lat} (**Figure 5d**). At 27 °C, the in-plane κ_{lat_xx} (κ_{lat_yy}) reaches an exceptionally high value of 33.74 W/(m·K) within the FeSe layers, whereas κ_{lat_zz} is only 1.09 W/(m·K), resulting in an extremely large anisotropy ratio of ~33. In contrast, $TlFe_{1.6}Se_2$ exhibits intrinsically suppressed κ_{lat} even along the in-plane direction (**Figure 5c**). At 27 °C, κ_{lat_xx} (κ_{lat_yy}) is only 1.43 W/(m·K), more than an order of magnitude lower than that of FeSe, while κ_{lat_zz} is further reduced to 0.42 W/(m·K).

To facilitate comparison with the experimental data for anisotropic polycrystalline

View Article Online
DOI: 10.1039/D5TA02075E

materials, we evaluated orientation-averaged κ_{lat} values using both a harmonic-mean (series-type) average, $\kappa_{lat}^{series} = (\frac{1}{\kappa_{xx}} + \frac{1}{\kappa_{yy}} + \frac{1}{\kappa_{zz}})^{-1} \times 3$, and an arithmetic-mean (parallel-type) average, $\kappa_{lat}^{parallel} = \frac{\kappa_{xx}+\kappa_{yy}+\kappa_{zz}}{3}$, which are plotted together with the measured κ_{lat} of V_{Fe}-ordered $TlFe_{1.6}Se_2$ and FeSe polycrystals (**Figures 5c,d**). The parallel-type average corresponds to a transport regime in which heat flows independently along different crystallographic directions, whereas the series-type average represents a transport regime largely controlled by the lowest κ_{lat} component. Both $TlFe_{1.6}Se_2$ and FeSe polycrystal exhibits κ_{lat} close to the κ_{lat}^{series}, indicating that heat transport in the polycrystalline form is largely governed by the low out-of-plane component. In FeSe, the intrinsically high in-plane κ_{lat} is strongly suppressed in the polycrystal, whereas in $TlFe_{1.6}Se_2$, the already low in-plane κ_{lat} is further reduced by the out-of-plane contribution.

Figures 5e,f compare the anisotropic frequency-resolved κ_{lat} at T = 300 K for $TlFe_{1.6}Se_2$ and FeSe, while the frequency-dependent cumulative κ_{lat} are shown in **Figures 5g,h**. In FeSe, the in-plane κ_{lat_xx} (κ_{lat_yy}) exhibits a pronounced peak around ~1.5 THz, whereas the out-of-plane κ_{lat_zz} shows a small peak at ~0.5 THz (**Figure 5f**). As shown in **Figure 5h**, phonons below ~5 THz account for about 90% of the total κ_{lat_xx} (κ_{lat_yy}), indicating that heat transport is dominated by acoustic phonon modes. The contribution to κ_{lat_zz} is confined to frequencies below ~1.5 THz and arises almost exclusively from acoustic phonons, reflecting intrinsically inefficient thermal transport along the out-of-plane direction. This anisotropic behavior is consistent with the steep phonon branches along the Γ–X and Γ–M directions, arising from highly dispersive in-plane acoustic phonons of the Fe-Se framework, and the much less dispersive phonon branches along the Γ–Z direction, reflecting the layered structural characteristic (**Figure 5b**).

For $TlFe_{1.6}Se_2$, the frequency-resolved κ_{lat} shows a clear directional contrast (**Figure 5e**). The in-plane κ_{lat_xx} (κ_{lat_yy}) spans a much broader frequency range extending up to ~10 THz,

View Article Online
DOI: 10.1039/D5TA02075E

mainly associated with the vibration of the Fe–Se framework (left panel of **Figure 5a**). In contrast, the out-of-plane κ_{lat_zz} is dominated by phonons below ~2 THz, primarily arising from the vibrations of the heavy Tl atoms (left panel of **Figure 5a**). The cumulative κ_{lat} (**Figure 5g**) further clarifies this difference. Below 2.5 THz, only ~49% of κ_{lat_xx} (κ_{lat_yy}) is accumulated, whereas more than ~96% of κ_{lat_zz} is contributed within this range. This indicates that higher-frequency optical modes contribute to more than half of the in-plane heat transport in $TlFe_{1.6}Se_2$. Such behavior is markedly different from FeSe, where in-plane heat transport is dominated almost entirely by low-frequency phonons. Consequently, the contribution of low-frequency phonons to κ_{lat_xx} (κ_{lat_yy}) is strongly suppressed in $TlFe_{1.6}Se_2$.

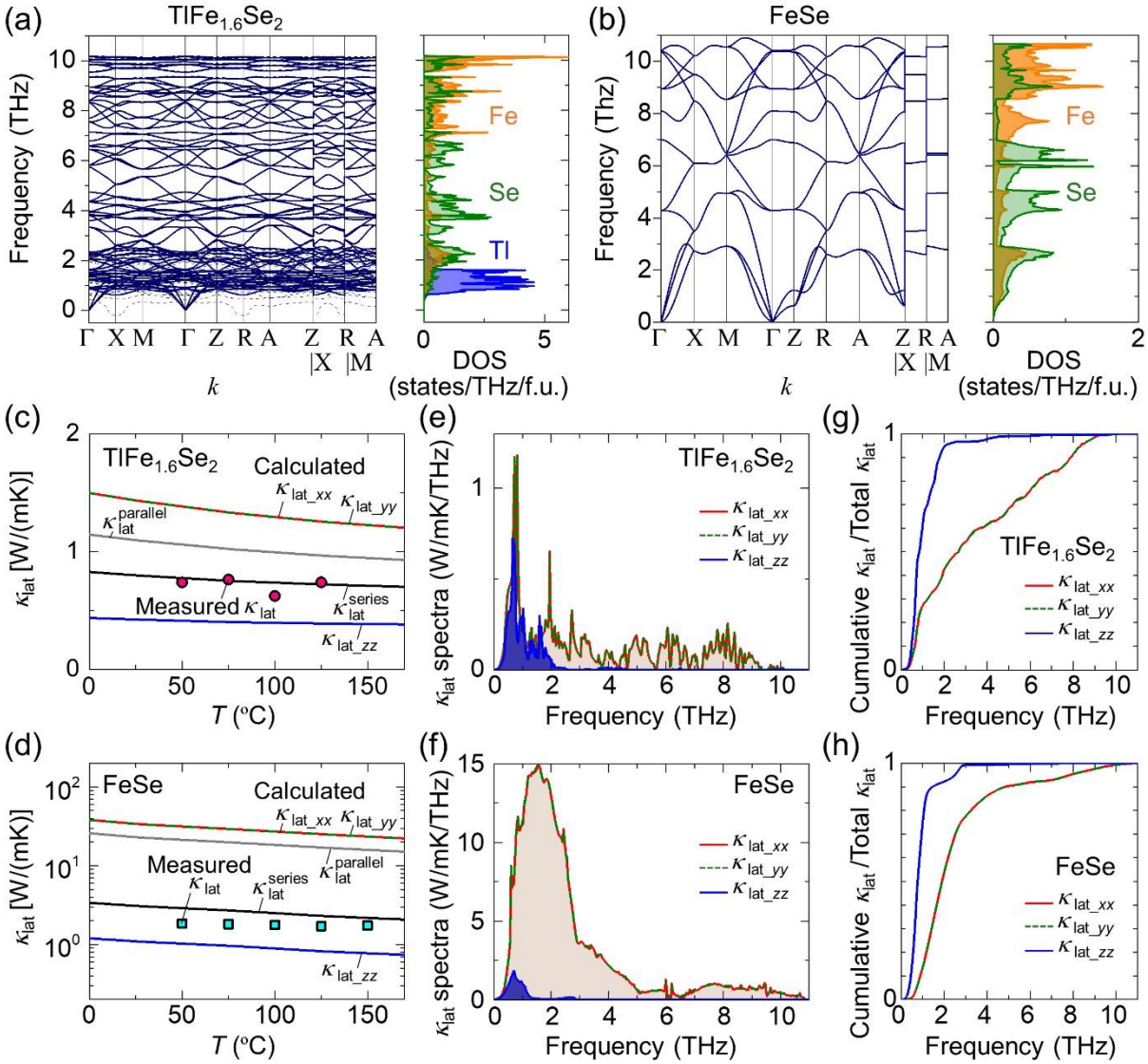

View Article Online
DOI: 10.1039/D5TA02075E

Figure 5. (a,b) Anharmonic phonon dispersions (left panels) and partial phonon density of states (DOSs) projected on each element (right panels) for (a) $TlFe_{1.6}Se_2$ and (b) FeSe at T = 300 K. The dotted black lines in (a) represent the phonon dispersion calculated within the harmonic approximation. The k-path is Γ (0.0, 0.0, 0.0), X (0.0, 0.5, 0.0), M (0.5, 0.5, 0.0), Z (0.0, 0.0, 0.5), R (0.0, 0.5, 0.5), and A (0.5, 0.5, 0.5). (c,d) T dependence of the calculated κ_{lat} along xx- and yy-axes (parallel to FeSe layer) and the zz-axis (perpendicular to FeSe layer) for (c) $TlFe_{1.6}Se_2$ and (d) FeSe. The averaged κ_{lat} values obtained using the series conduction model ($\kappa_{lat}^{series} = (\frac{1}{\kappa_{xx}} + \frac{1}{\kappa_{yy}} + \frac{1}{\kappa_{zz}})^{-1} \times 3$) and the parallel conduction model ($\kappa_{lat}^{parallel} = \frac{\kappa_{xx}+\kappa_{yy}+\kappa_{zz}}{3}$) are also shown. The experimentally measured κ_{lat} for V_{Fe}-ordered $TlFe_{1.6}Se_2$ and FeSe polycrystals are also plotted for comparison. (e,f) Comparison of κ_{lat} spectra for (e) $TlFe_{1.6}Se_2$ and (f) FeSe at T = 300 K. (g,h) Frequency-dependent cumulative κ_{lat} for (g) $TlFe_{1.6}Se_2$ and (h) FeSe at T = 300 K.

Figure 6 compares the phonon group velocity (ν_{ph}), phonon lifetime (τ_{ph}), and phonon mean free path (l_{ph}) as functions of phonon frequency. $TlFe_{1.6}Se_2$ exhibits much lower ν_{ph} than FeSe over wide frequency range (**Figure 6a**), reflecting the flatter acoustic and optical phonon branches shown in **Figure 5a**. This reduction in ν_{ph} originates from the weak coupling between the heavy Tl atoms and the Fe–Se framework, which effectively softens the lattice vibrations and limits phonon propagation. More importantly, τ_{ph} in $TlFe_{1.6}Se_2$ is reduced over a broad frequency range, with an exceptionally strong suppression observed for phonons below ~4 THz (**Figure 6b**). In the lowest-frequency region below ~1.5 THz, this reduction is primarily associated with Tl-related vibrational modes, whereas in the higher-frequency region up to ~4 THz it mainly affects phonons derived from the Fe–Se framework. As a result, l_{ph} in $TlFe_{1.6}Se_2$ is strongly suppressed particularly because the τ_{ph} of phonon modes below ~4 THz become extremely short (**Figure 6c**). These results indicate that two distinct scattering mechanisms

View Article Online
DOI: 10.1039/D5TA02075E

operate in different frequency regimes: low-frequency phonon scattering induced by the weakly bound heavy Tl atoms, and additional scattering of Fe–Se framework phonons in $TlFe_{1.6}Se_2$.

To further clarify the microscopic origin of the enhanced phonon scattering in Fe–Se framework, we evaluated the Fe–Se bonding characteristics in $TlFe_{1.6}Se_2$ and FeSe by estimating their bonding energies using crystal orbital Hamilton population (COHP)[43] analysis, as implemented in the LOBSTER code.[44] The −iCOHP values, obtained by integrating −COHP up to the Fermi level and corresponding to the bond strength, are 2.35 eV per bond for Fe–Se bonds in FeSe and range from 2.17 to 2.51 eV per bond in $TlFe_{1.6}Se_2$, with an average value of 2.34 eV per bond. The Fe–Se bond length in FeSe is 2.278 Å, while that in $TlFe_{1.6}Se_2$ spans a range of 2.242–2.290 Å, yielding an average bond length of 2.272 Å (**Figure S6** in Supporting Information). These results indicate that the average Fe–Se bond strength and bond length are nearly identical in $TlFe_{1.6}Se_2$ and FeSe. In contrast, $TlFe_{1.6}Se_2$ exhibits a pronounced distribution of Fe–Se bond strengths, reflecting bond heterogeneity induced by V_{Fe} ordering. Such bond heterogeneity provides an additional phonon-scattering channel, particularly for intermediate- and high-frequency Fe–Se vibrational modes, and plays a key role in shortening τ_{ph} and suppressing κ_{lat}. This is further supported by the interatomic force constant (IFC) distributions (**Figure S7** in Supporting Information), showing the broadened force-constant distribution in $TlFe_{1.6}Se_2$ compared to FeSe. In addition, the three-phonon scattering phase space (SPS) is significantly enhanced, particularly in the 1.5–4 THz region (**Figure S8** in Supporting Information), indicating an increased number of scattering channels in this frequency range. This frequency range is dominated by Fe–Se vibrational modes with strong acoustic–optical mixing (**Figure 5a**), making them sensitive especially to the bond heterogeneity. The dominance of force-constant disorder is inferred also from the frequency-selective reduction of phonon lifetimes between 1.5 and 4 THz (**Figure 6b**). Therefore, the lifetime reduction in this frequency window is primarily driven by emission channels activated by force-constant disorder, while mass disorder provides a secondary background contribution.

View Article Online
DOI: 10.1039/D5TA02075E

Such bond-heterogeneity-induced phonon scattering has also been reported in a variety of complex crystalline materials, where local fluctuations in bonding strength or force constants give rise to enhanced anharmonic phonon scattering and reduced κ_{lat}.[45-49] In the V_{Fe}-disordered phase, this bond heterogeneity is further amplified by the random distribution of V_{Fe}, introducing additional mass and force-constant disorder. This disorder-driven enhancement of phonon scattering accounts for the further reduction of κ_{lat} observed experimentally at elevated temperatures. Direct first-principles calculations for V_{Fe} disordered phases were not performed due to the large configurational space associated with random vacancy distributions and limitation of our computational resource. Random V_{Fe} distributions are expected to introduce spatially uncorrelated force-constant disorder, which is likely more effective in scattering phonons than the ordered structure, leading to additional suppression of κ_{lat}.

View Article Online
DOI: 10.1039/D6TA02075E

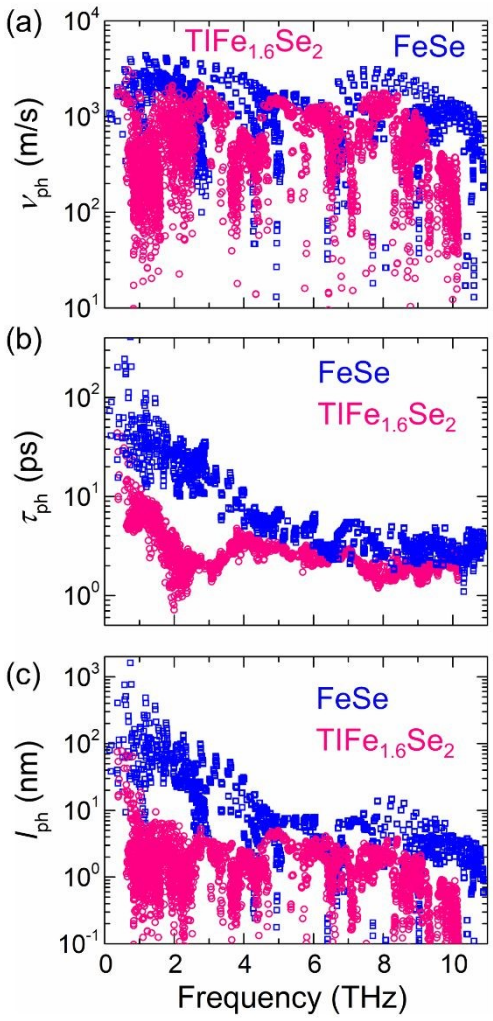

Figure 6. (a) Phonon group velocity (v_{ph}), (b) phonon lifetime (τ_{ph}), and (c) phonon mean free path (l_{ph}) in terms of the phonon frequency for $TlFe_{1.6}Se_2$ (pink plots) and FeSe (blue plots) at T = 300 K.

4 Conclusions

We investigated the thermoelectric properties of layered $TlFe_{1.6}Se_2$, motivated by the expectation that its embedded two-dimensional FeSe transport layers, together with the V_{Fe} order–disorder transition, could provide a unique combination of enhanced PF and suppressed κ_{lat}. $TlFe_{1.6}Se_2$ exhibited an exceptionally low κ_{lat}, reaching ~0.7 W/(mK) in the V_{Fe}-ordered phase at 50 °C and further decreasing to ~0.2 W/(mK) in the V_{Fe}-disordered phase at 500 °C, which is comparable to or even lower than those of high-performance thermoelectric materials

with intrinsically low κ_{lat}. Notably, unlike layered FeSe, which shows extremely high in-plane κ_{lat} and strong anisotropy, κ_{lat} in $TlFe_{1.6}Se_2$ is intrinsically suppressed even along the in-plane direction. This ultralow κ_{lat} originates from the combined effects of weakly bound heavy Tl atoms, which reduce phonon group velocities, and enhanced phonon scattering caused by V_{Fe}-induced bond heterogeneity within the Fe–Se framework.

The electronic transport properties are strongly modulated across the transition between V_{Fe} ordered and disordered states. In the V_{Fe}-disordered phase, $TlFe_{1.6}Se_2$ exhibits a metallic state with enhanced σ and ultralow κ_{lat}; however, strong carrier compensation significantly reduces the S, limiting the ZT value to ~0.05. In contrast, in the V_{Fe}-ordered phase, the opening of a Mott gap leads to a large S of ~110 μV/K at 50 °C, resulting in an enhanced PF of 5.2 μW/(cmK^2) and a ZT of ~0.2. These results demonstrate that the confinement of FeSe layers within bulk $TlFe_{1.6}Se_2$ enables a substantial PF enhancement compared with bulk FeSe, while V_{Fe} ordering and disordering play a complementary role by tuning carrier transport and strongly suppressing κ_{lat}. Looking forward, further enhancement of ZT may be achieved by optimizing the carrier concentration in the V_{Fe}-ordered phase and by tuning the V_{Fe} concentration.

Although the incorporation of two-dimensional FeSe layers suggested the possibility of achieving a high PF comparable to that of FeSe monolayers, the obtained PF is substantially lower. This difference is primarily attributed to the much lower carrier mobility in $TlFe_{1.6}Se_2$, which is about four orders of magnitude smaller than that of FeSe monolayers, likely due to the polycrystalline nature and enhanced carrier scattering arising from V_{Fe} ordering/disordering and interactions involving Tl atoms. In contrast, the exceptionally high mobility in FeSe monolayers is realized for in-plane transport in the two-dimensional electronic structure. To clarify the intrinsic transport properties and to potentially realize higher PF in $TlFe_{1.6}Se_2$, studies using single crystals or epitaxial thin films will be essential, as they enable selective probing of in-plane transport in the embedded FeSe layers.

Extending this concept to other alkali-based $A_{1-x}Fe_{2-y}Se_2$ (A = K, Rb, Cs) is an attractive

View Article Online
DOI: 10.1039/D6TA02075E

direction, as they consist of FeSe layers with V_{Fe}, forming quasi-two-dimensional frameworks, and exhibit high electrical conductivity. Moreover, these systems show high-T_c superconductivity, reminiscent of FeSe monolayers, suggesting a close connection between their electronic structures. In addition, the V_{Fe} concentration in these systems can be tuned over a wide range,[16,17] providing a versatile platform for controlling carrier concentration and optimizing thermoelectric performance. However, their poor air stability, precise control of vacancy ordering, and suppression of phase separation remain significant challenges.[15] The growth of high-quality single crystals or epitaxial thin films will also be essential to clarify intrinsic transport properties. A possible strategy to address air stability is partial substitution or solid-solution formation with air-stable Tl-based compounds,[50] which may enable simultaneous control of environmental stability and thermoelectric performance.

Taken together, the present study highlights the confinement of two-dimensional FeSe layers, combined with vacancy-order control, as a promising design strategy for bulk thermoelectric materials that combine large PF with intrinsically low κ_{lat}.

View Article Online
DOI: 10.1039/D6TA02075E

Conflicts of interest

There are no conflicts to declare.

Data availability

The data supporting this article are included within the article and its Supplementary Information. Supporting information: bulk synthesis, characterization, and theoretical calculations for $TlFe_{1.6}Se_2$ and FeSe.

Acknowledgements

This work was supported by MEXT Program: Data Creation and Utilization Type Material Research and Development Project (Grant No. JPMXP1122683430), Design and Engineering by Joint Inverse Innovation for Materials Architecture, and also by a project of Kanagawa Institute of Industrial Science and Technology (KISTEC). X. He was supported by Japan Society for the Promotion of Science (JSPS) through Grant-in-Aid for Research Activity Start-up (Grant No. 25K23539). T. Katase was supported by Special Award for Science Tokyo Advanced Researchers (STAR) funded by Institute of Science Tokyo and JSPS through Grant-in-Aids for Scientific Research (B) (Grant No. 26K01206), Scientific Research (A) (Grant No. 24H00314), Scientific Research (S) (Grant No. 22H04964), and Challenging Research (Exploratory) (Grant No. 24K21671). H.Hi. was supported by JSPS through Grants-in-Aid for Scientific Research (A) (Grant Nos. JP20H00302, JP21H04612, and JP24H00376). The numerical calculations were carried out on the TSUBAME3.0 supercomputer at Institute of Science Tokyo supported by the MEXT Project of the Tokyo Tech Academy for Convergence of Materials and Informatics (TAC-MI), and the supercomputer at Research Center for Computational Science, Okazaki, Japan. The crystal structures in **Figure 1** were drawn using the VESTA code.[51]

References

1 F. J. DiSalvo, *Science*, 1999, **285**, 703–706.

2 L. E. Bell, *Science*, 2008, **321**, 1457–1461.

3 Q. H. Zhang, X. Y. Huang, S. Q. Bai, X. Shi, C. Uher, and L.D. Chen, *Adv. Eng. Mater.*, 2016, **18**, 194–213.

4 G. J. Snyder and E. S. Toberer, *Nat. Mater.*, 2008, **7**, 105–114.

5 S. Shimizu, J. Shiogai, N. Takemori, S. Sakai, H. Ikeda, R. Arita, T. Nojima, A. Tsukazaki, and Y. Iwasa, *Nat. Commun.*, 2019, **10**, 825.

6 F.-C. Hsu, J.-Y. Luo, K.-W. Yeh, T.-K. Chen, T.-W. Huang, P. M. Wu, Y.-C. Lee, Y.-L. Huang, Y.-Y. Chu, D.-C. Yan, and M.-K. Wu, *Proc. Natl. Acad. Sci.*, 2008, **105**, 14262–14264.

7 J.-F. Ge, Z.-L. Liu, C. Liu, C.-L. Gao, D. Qian, Q.-K. Xue, Y. Liu, and J.-F. Jia, *Nat. Mater.*, 2014, **14**, 285–289.

8 Y. Machida, K. Tomokuni, T. Isono, Y. Nakajima, and T. Tamegai, *J. Phys. Soc. Jpn.*, 2009, **78**, 073705.

9 J. G. Checkelsky, R. Thomale, L. Li, G. F. Chen, J. L. Luo, N. L. Wang, and N. P. Ong, *Phys. Rev. B*, 2012, **86**, 180502(R).

10 P. Devi Lodhi, N. Kaurav, K. K. Choudhary, and Y. K. Kuo, *J. Low Temp. Phys.*, 2019, **196**, 494–509.

11 C. B. Satterthwaite and R. W. Ure, *Phys. Rev.*, 1957, **108**, 1164–1170.

12 F. Ye, S. Chi, W. Bao, X. F. Wang, J. J. Ying, X. H. Chen, H. D. Wang, C. H. Dong, and M. Fang, *Phys. Rev. Lett.*, 2011, **107**, 137003.

13 R. Yu, J.-X. Zhu, and Q. Si, *Phys. Rev. Lett.*, 2011, **106**, 186401.

14 X.-W. Yan, M. Gao, Z.-Y. Lu, and T. Xiang, *Phys. Rev. Lett.*, 2011, **106**, 087005.

15 W. Li, H. Ding, P. Deng, K. Chang, C. Song, K. He, L. Wang, X. Ma, J.-P. Hu, X. Chen, and Q.-K. Xue, *Nat. Phys.*, 2012, **8**, 126–130.

16 J. Guo, S. Jin, G. Wang, S. Wang, K. Zhu, T. Zhou, M. He, and X. Chen, *Phys. Rev. B*, 2010, **82**, 180520.

17 Y. J. Yan, M. Zhang, A. F. Wang, J. J. Ying, Z. Y. Li, W. Qin, X. G. Luo, J. Q. Li, J. Hu, and X. H. Chen, *Sci. Rep.*, 2012, **2**, 212.

18 B. C. Sales, M. A. McGuire, A. F. May, H. Cao, B. C. Chakoumakos, and A. S. Sefat, *Phys Rev B*, 2011, **83**, 224510.

19 A. F. May, M. A. McGuire, H. Cao, I. Sergueev, C. Cantoni, B. C. Chakoumakos, D. S. Parker, and B. C. Sales, *Phys. Rev. Lett.*, 2012, **109**, 077003.

20 T. Katase, H. Hiramatsu, T. Kamiya, and H. Hosono, *Proc. Natl. Acd. Sci.*, 2014, **111**, 3979–3983.

21. H. J. Goldsmid, Introduction to Thermoelectricity, Springer, Heidelberg, 2009.

22 X. He, S. Kimura, T. Katase, T. Tadano, S. Matsuishi, M. Minohara, H. Hiramatsu, H. Kumigashira, H. Hosono, and T. Kamiya, *Adv. Sci.*, 2023, **11**, 2307058.

23 G. Kresse and D. Joubert, *Phys. Rev. B*, 1999, **59**, 1758–1775.

24 G. Kresse, and J. Furthmüller, *Phys. Rev. B*, 1996, **54**, 11169–11186.

25 J. P. Perdew, A. Ruzsinszky, G. I. Csonka, O. A. Vydrov, G. E. Scuseria, L. A. Constantin, X. Zhou, and K. Burke, *Phys. Rev. Lett.*, 2008, **100**, 136406.

26 T. Tadano, and S. Tsuneyuki, *Phys. Rev. B*, 2015, **92**, 054301.

27 T. Tadano, Y. Gohda, and S. Tsuneyuki, *J. Phys.: Condens. Matter*, 2014, **26**, 225402.

28 G. Kresse, J. Furthmüller, and J. Hafner, *Europhys. Lett.*, 1995, **32**, 729−734.

29 K. Parlinski, Z. Li, and Y. Kawazoe, *Phys. Rev. Lett.*, 1997, **78**, 4063−4066.

30 T. Tadano and S. Tsuneyuki, *Phys. Rev. B*, 2015, **92**, 054301.

31 M. Simoncelli, N. Marzari, and F. Mauri, *Nat. Phys.*, 2019, **15**, 809–813.

32 S. Tamura, *Phys. Rev. B*, 1983, **27**, 858–866.

33 H. Cao, C. Cantoni, A. F. May, M. A. McGuire, B. C. Chakoumakos, S. J. Pennycook, R. Custelcean, A. S. Sefat, and B. C. Sales, *Phys. Rev. B*, 2012, **85**, 054515.

34 G. Li, B. Zhang, T. Baluyan, J. Rao, J. Wu, A. A. Novakova, P. Rudolf, G. R. Blake, R. A. de Groot, T. T. M. Palstra, *Inorg. Chem.* 2016, **55**, 12912–12922.

35 T. M. McQueen, Q. Huang, V. Ksenofontov, C. Felser, Q. Xu, H. Zandbergen, Y. S. Hor, J. Allred, A. J. Williams, D. Qu, J. Checkelsky, N. P. Ong, and R. J. Cava, *Phys. Rev. B*, 2009, **79**, 014522.

36 M. Kawai, F. Nabeshima, and A. Maeda, *J. Phys.: Conf. Ser.*, 2018, **1054**, 012023.

37 G. J. Snyder, A. H. Snyder, M. Wood, R. Gurunathan, B. H. Snyder, C. Niu, *Adv. Mater.*, 2020, **32**, 2001537.

38 T. Zhu, Z. Xu, J. He, J. Shen, S. Zhu, L. Hu, T. M. Tritt, and X. Zhao, *J. Mater. Chem. A*, 2013, **1**, 11589–11594.

39 Q. Zhang, F. Cao, W. Liu, K. Lukas, B. Yu, S. Chen, C. Opeil, D. Broido, G. Chen, Z. Ren, *J. Am. Chem. Soc.*, 2012, **134**, 10031–10038.

40 Q. Zhang, Z. Ti, Y. Zhu, Y. Zhang, Y. Cao, S. Li, M. Wang, D. Li, B. Zou, Y. Hou, P. Wang, and G. Tang, *ACS Nano*, 2021, **15**, 19345–19356.

41 M. Li, S. M. Kazi Nazrul Islam, M. Yahyaoglu, D. Pan, X. Shi, L. Chen, U. Aydemir, and

View Article Online
DOI: 10.1039/D6TA02075E

X. Wang, *Info. Mat.*, 2019, **1**, 108.

42 C. Zhou, Y. K. Lee, Y. Yu, S. Byun, Z.-Z. Luo, H. Lee, B. Ge, Y.-L. Lee, X. Chen, J. Y. Lee, O. Cojocaru-Mirédin, H. Chang, J. Im, S.-P. Cho, M. Wuttig, V. P. Dravid, M. G. Kanatzidis, and I. Chung, *Nat. Mater.*, 2021, **20**, 1378–1384.

43 R. Dronskowski and P. E. Bloechl, *J. Phys. Chem.*, 1993, **97**, 8617.

44 S. Maintz, V. L. Deringer, A. L. Tchougréeff, and R. Dronskowski, *J. Comput. Chem.*, 2016, **37**, 1030.

45 T. Katase, N. Sato, and T. Mori, *Appl. Phys. Rev.*, 2025, **12**, 041319.

46 D. T. Morelli, V. Jovovic, and J. P. Heremans, *Phys. Rev. Lett.*, 2008, **101**, 035901.

47 M. Dutta, K. Pal, U. V. Waghmare, and K. Biswas, *Chem. Sci.*, 2019, **10**, 4905–4913.

48 N. Sato, N. Kuroda, S. Nakamura, Y. Katsura, I. Kanazawa, K. Kimura, and T. Mori, *J. Mater. Chem. A*, 2021, **9**, 22660–22669.

49 X. He, S. Nomoto, T. Komatsu, T. Katase, T. Tadano, S. Kitani, H. Yoshida, T. Yamamoto, H. Mizoguchi, K. Ide, H. Hiramatsu, H. Kawaji, H. Hosono, and T. Kamiya, *Adv. Funct. Mater.*, 2023, 33, 2213144.

50 M.-H. Fang, H.-D. Wang, C.-H. Dong, Z.-J. Li, C.-M. Feng, J. Chen, H. Q. Yuan, *Europhys. Lett.* 2011, **94**, 27009.

51 K. Momma and F. Izumi, *J. Appl. Crystallogr.*, 2011, **44**, 1272–1276.

View Article Online
DOI: 10.1039/D6TA02075E

Data availability

The data supporting this article are included within the article and its Supplementary Information.